Chipless RFID Based on Micro-Doppler Effect

Ashkan Azarfar, Nicolas Barbot, Etienne Perret

Chipless RFID based on Micro-Doppler Effect

Ashkan Azarfar, *Member, IEEE,* Nicolas Barbot, *Member, IEEE,* and Etienne Perret, *Senior Member, IEEE*

***Abstract*—This paper demonstrates how motion effect can be exploited to read moving chipless RFID tags at larger distances compared to what has been reached without benifitly taking into account the movement. According to the Doppler effect, due to the time-variant behaviour of moving chipless tags, the tag back-scattered field contains frequency components different from those are transmitted. These motion-induced frequency components can be utilized to efficiently detect the tag at large distances, in a real environment composed of stationary objects. A circuit based analytical model verified by full-wave simulations, is presented to effectively predict the quasi-stationary back-scattered field from moving scatterers, with fast computation process. The developed analytic model is applied to rotating dipole scatterers and is used to design chipless tags including an identifier. In term of identification, good agreement is observed between the measurement results and those are predicted by the model. Finally, read range enhancement is proved experimentally by a real environment measurement where the chipless tags are readable at distances up to several meters.**

***Index Terms*—Chipless RFID, Doppler effect, RCS, read range, scatterers.**

I. Introduction

CHIPLESS technology has been introduced as an effective way to reduce the cost of traditional Radio Frequency IDentification (RFID). Since the tag does not rely on a silicon chip, fabrication cost can significantly be lowered. Moreover, this technology is also compatible with mass production. In this regard, different printing techniques have been utilized to implement low-cost and compact chipless RFID tags [1]–[3]. However, removing the chip also add important side effect to store and transmit the ID of the tag to the reader. Over the past decades, researchers have developed efficient mechanism to encode the information [4]–[8], to decrease the size of the tag [9], and to integrate chipless technology in sensor applications [10]–[13]. Despite these efforts, read range of chipless tag remains lower than the one achieved in classical UHF tags.

Chipless read range has been investigated in the literature, however, most of the studies are limited by a range lower than 1 m. Several notable exception works have been done to increase chipless read range based on the use of highly directive reader antennas to focus the beam toward the tags [14]–[16]. Nevertheless, all these designs suffer from severe misalignment constraints which limit their use in practical applications.

A study was conducted in [17], and shows that read range of chipless technology is in fact limited since chipless tags are Linear Time-Invariant (LTI) systems. Actually, as the EM interaction with the chipless tag and almost all material in the background environment can be modeled by LTI systems, the back-scattered signals from both tag and the environment share the same frequencies as the transmitted signal. Accordingly, chipless tags can not be differentiated easily from objects present in the environment which drastically decreases the read range. In addition, increasing the transmitted power can not help to enhance the read range. The only way to significantly increase the read range is to break the LTI property associated to the chipless tags. This result can be achieved by two independent ways as follows. The first solution is to add a non-linear element (such as a diode) into the tag structure. Note that in this case, the tag is not really a chipless tag anymore but a harmonic transponder [18], [19]. The second approach is to break the time-invariant property. Movement can be considered as an effective feasible solution to violate time-invariance for chipless tags when they are attached to objects with even small displacements. Basically, scattering from objects with micro-motions has been widely studied as micro-Doppler effect [20]. This principle has been recently used in [21] to detect a rotating beacon but without identification capabilities. In [22], the polarimetric scattering response of the chipless tag is modified during a rotational movement, however, this principle is not related to micro-Doppler effect.

The micro-Doppler signature [23] of the targets with rotating and vibrating parts such as multi-copter drones [24]–[26] and human body [27]–[29] have been widely studied for classification goal. In these works, since the back-scattering profile of the targets are unknown it is necessary to use a time-consuming and complex classification process based on data mining and machine learning methods like artificial neural networks. In contrast, in micro-Doppler based chipless technology, tag IDs are known and predefined for the reader which makes it possible to identify the tag with only one measurement from a large distance. Moreover, in most of the above-mentioned works, the frequency-dependent and polarimetric scattering response of the moving parts have not been investigated with an analytical model causing to miss a portion of information which is utilized by our proposed solution to retrieve the ID from a moving chipless tag.

In the case of translational movement, chipless tagged objects carried by a conveyor belt have been read robustly in [30] while the interrogation range is still limited by 1 m. Actually, in [30] since the data have been captured from chipless tags in different locations using short-time pulses without considering the Doppler effect, the processing procedure has not been able to overcome the limitations caused by LTI properties associated to stationary chipless tags.

This paper, as an extended version of [31], demonstrates the promising prospects of chipless read range enhancement and identification by exploiting the micro-Doppler effect. The proposed approach can be applied for any application in which the tagged objects are in movement. The paper is

Authors are with Grenoble INP, France.

This is an expanded version of the original paper presented in 2021 IMS.

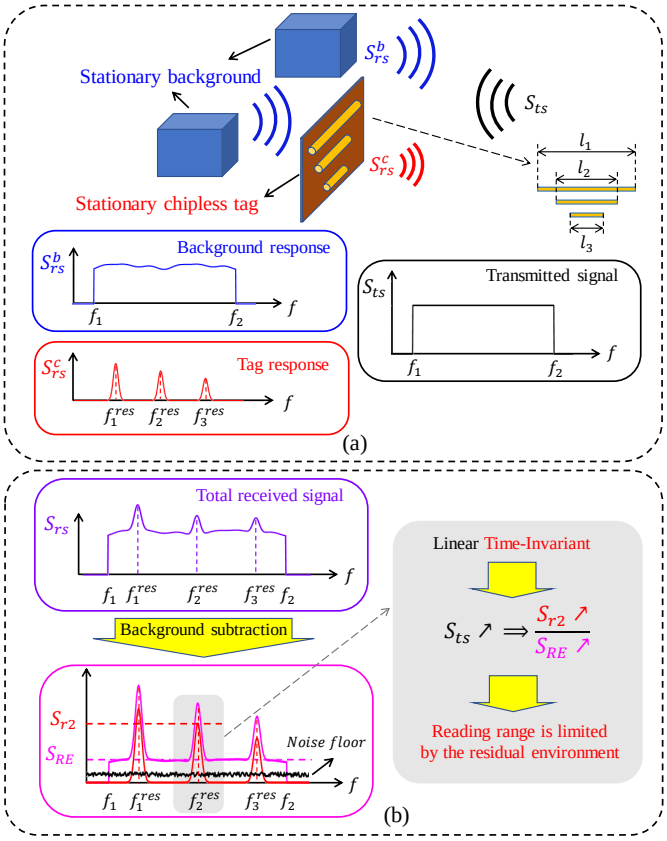

Fig. 1. (a) Classical communication scenario to identify stationary chipless tags. (b) Detection process with limited reading range due to the residual environment response.

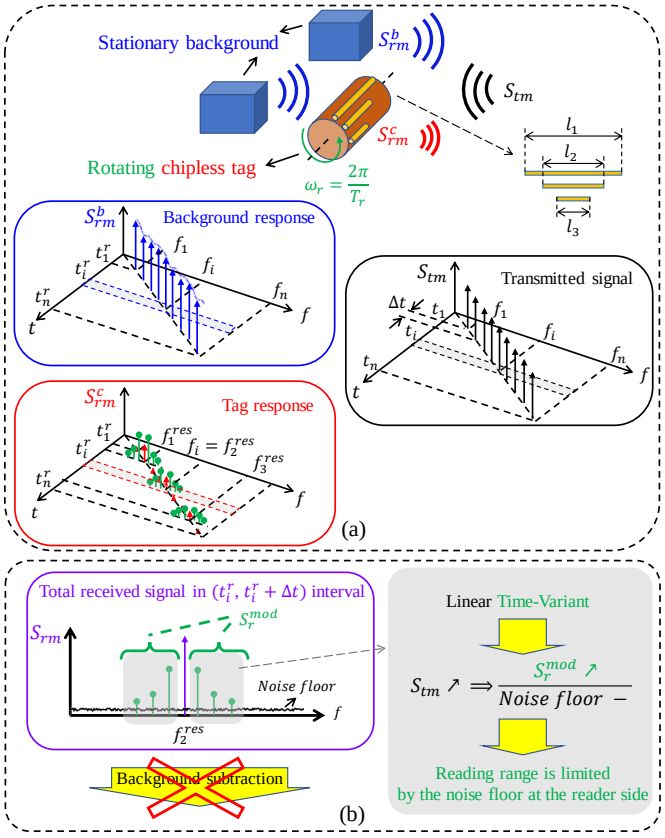

Fig. 2. (a) Proposed communication process to identify a rotating chipless tag. (b) Motion-induced modulated signal allows to increase the detection range.

organized as follows. Section II illustrates the concept by doing a comparison between stationary and moving chipless tags. In Section III, an analytical model is developed to predict scattering from single and multiple rotating resonant dipoles, and the model is verified by simulation. Section IV presents the measurement results in terms of tag identification and especially increased read range. Finally, Section V concludes the paper.

II. Moving vs. Stationary Chipless Tags

The communication scenario classically used to identify a chipless tag is presented in Fig. 1(a). In this example, the stationary chipless tag consists of three short-circuited dipole scatterer with different lengths of l_1, l_2 and l_3 which resonate at the frequencies of f_1^{res}, f_2^{res} and f_3^{res} respectively. Usually, the chipless tag should be identified in a real environment in which some other objects are present. These objects can be considered as almost stationary bodies that have been shown by the blue cubes in Fig. 1(a). In addition, these background objects are mostly composed of materials with linear electromagnetic properties like metals and dielectric substances. To identify the chipless tag, commonly, a UWB signal as S_{ts} is transmitted and the spectrum of the received signal will be investigated for identification. As both chipless tag and background objects are linear in terms of electromagnetic properties, the total EM back-scattered signal (S_{rs}) can be considered as the superposition of the background response (S_{rs}^b) and the chipless tag response (S_{rs}^c) which has three peaks associated to the three resonating dipole scatterers. Furthermore, since both tag and background objects are supposed to be stationary in time, both contributions can be modeled by LTI systems which fundamentally do not generate any new frequency components in the response. Thus, the total back-scattered signal (S_{rs}) has exactly the same frequency components as those of the transmitted signal. In other words, if a continuous wave is sent from the reader, the received wave is at the same frequency. Mostly, to isolate the tag response from the total response for easy detection, a complex subtraction is done with the background response (same environment but with the tag removed). However, due to the intrinsic randomness of the real environment, it is not possible to perfectly remove the contribution of the background and so, a residual response (S_{RE}) will always remain which limit the reading range of any stationary chipless tag [17]. For example, this fact has been simply shown in Fig. 1(b) for the second dipole at f_2^{res}. Due to the LTI properties, if the amplitude of the transmitted signal increases, both tag and the residual response will increase with the same scales which causes the reading range to be limited by the residual response instead of the minimum required Signal-to-Noise Ratio (SNR) level at the reader side. Thus, read range can not be enhanced by increasing the transmitted power.

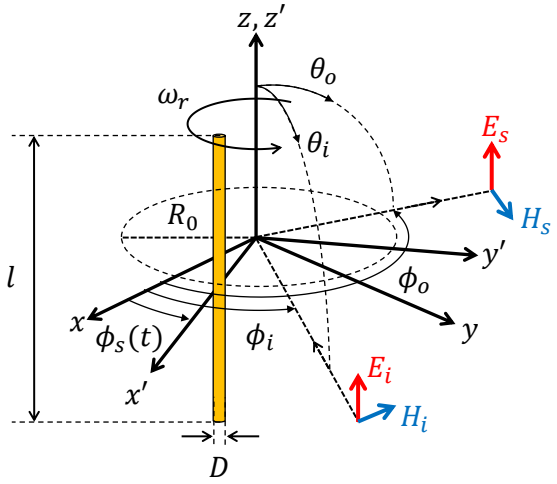

Fig. 3. Rotating short-circuited dipole impinged by a time-harmonic linearly z-polarized plane wave.

In [17], it has been clearly demonstrated that breaking the linearity or time-invariability of the chipless tags are the only ways which help to significantly increase their reading range. Specifically, in this work, the time-invariability will be violated by taking into account the effect of the motion. Rotation as an easily-implemented and regular motion has been considered here to demonstrate the concept. But of course, as long as the motion trajectory of the chipless tag can be approximated well, this approach is applicable. Fig. 2(a) presents the proposed communication process to identify a rotating chipless tag. Here, the same three dipoles are mounted on a dielectric cylinder rotating with angular rotation frequency of ω_r=$2\pi/T_r$, and the stationary objects in the background are shown as before by the blue cubes in Fig. 2(a). It is important to mention that, the cylinder because of its perfect revolutional symmetry can be considered as a stationary object while rotating around its axis. So, except the rotating dipoles, all the other objects in the background are assumed stationary and contribute as background response. As an interrogating signal (S_{tm}), a time-stepped sequence of CW signals with frequencies of $f_1, ..., f_n$ is transmitted at times of $t_1, ..., t_n$ during a time interval Δt. Practically, Δt should be greater compared to the period of the rotation (T_r) to provide sufficient acquisition time in reception. As linearity is still maintained, the total back-scattered signal can be considered as the superposition of the tag (S^c_{rm}) and background (S^b_{rm}) responses. However, there is an essential difference here that the rotating chipless tag behaves as a Linear Time-Variant (LTV) system producing some new frequency components which definitely are not present in S^b_{rm}. For the tag response in Fig. 2(a), three non-zero red impulses associated to the resonance frequency of the dipoles are illustrated while, due to the resonating behaviour of the scatteres, the other carrier frequencies have been shown by zero-amplitude impulses. In addition, the newly generated frequency components are depicted by green impulses around the three resonance frequencies. Indeed, due the rotation, the scattered power from the dipoles has been modulated around the carrier frequencies at which dipoles resonate. For the same example as before, to detect the second dipole resonating at f_2^{res}, the modulated portion of the received signal (S_r^{mod}) will be considered which is benefitly not affected by the background response, as shown in Fig. 2(b). Accordingly, the background subtraction is not needed anymore and the reading range will not be limited by the residual response in this case. As it is illustrated in Fig. 2(b), in contrast to the stationary case, by increasing the amplitude of the transmitted signal, the modulated components (S_r^{mod}) will increase with the same scale while the noise floor level at the receiver remains constant. This feature makes it possible to detect the rotating chipless tag at larger distances without being limited by the residual environment response. Basically, this principle is identically used by the UHF RFID technologies where the chips modulate the back-scattered signal. Therefore, moving chipless tags can be expected to be read at large distances like UHF chipped tags.

III. Analytical Model and Simulations

A. Scattering from single rotating short-circuited dipole

Fig. 3 shows a short-circuited dipole with the length of l and diameter of D which is aligned with the z-axis and rotates around it. The radius of the rotation and the angular rotation frequency of the dipole are R_0 and $\omega_r = 2\pi f_r$, respectively. A time-harmonic plane wave at the frequency of f_0 with a linearly z-polarized electric field impinges on the rotating dipole at the incidence angle of (θ_i, ϕ_i), and the scattered field is considered at the observation angle of (θ_o, ϕ_o). The dipole is located on the x'-axis of the $x'y'z'$-coordinate system which is rotating with $\phi_s(t) = \omega_r t$ about the z-axis of the reference xyz-coordinate system.

To accurately model the scattering from moving objects, time-dependent Maxwell's equations should be considered with time-varying boundary conditions [32]. However, scattering by moving bodies in the presence of a time-harmonic plane wave can be approximated by a time-dependent sequence of stationary scattered fields, called quasi-stationary approximation [33], [34]. In most practical cases, where the maximum velocity of the moving object is much smaller than the velocity of the light in vacuum c_0, the quasi-stationary fields will provide a good approximation to the exact scattered fields [33]. Accordingly, using the quasi-stationary approximation, correct solution can be obtained by calculating the stationary fields scattered by the object at each time t while the object is "frozen" at the corresponding coordinate. This is a powerful approach to theoretically solve slowly time-varying boundary problems and also to obtain the solution by doing frequency-domain simulations. For the normal incidence ($\theta_i = \pi/2$), the incident electric field in the reference coordinate system is expressed as

$$\vec{E}_i(\vec{r}) = E_0 \; e^{jk(x\cos\phi_i + y\sin\phi_i)} \; \hat{z} \tag{1}$$

where k=$2\pi f_0/c_0$=$2\pi/\lambda$. Using the rotation transformation of $[r] = [R_t(\phi_s(t))][r']$ which can be written as

$$\begin{bmatrix} x \\ y \\ z \end{bmatrix} = \begin{bmatrix} \cos\phi_s(t) & -\sin\phi_s(t) & 0 \\ \sin\phi_s(t) & \cos\phi_s(t) & 0 \\ 0 & 0 & 1 \end{bmatrix} \begin{bmatrix} x' \\ y' \\ z' \end{bmatrix} \tag{2}$$

the expression of the incident field in the rotating coordinate system attached to the dipole can be obtained as

$$\vec{E_i}(\vec{r'}) = \hat{z}E_0\ e^{jkx'(\cos\phi_i\cos\phi_s+\sin\phi_i\sin\phi_s)} \times e^{jky'(-\cos\phi_i\sin\phi_s+\sin\phi_i\cos\phi_s)} \quad (3)$$

To obtain the quasi-stationary scattered field using the radiation integrals [35], it is sufficient to acquire the induced current on the short-circuited dipole in each time t during the rotation. For the normal incidence on the dipole, the induced current can be well approximated by

$$\begin{cases} I(z') = I_0 \sin\left(k(\frac{l}{2} - |z'|)\right) & 0 < l \leq \frac{3\lambda}{4} \quad (4a) \\ I(z') = 0 & \frac{3\lambda}{4} < l < \frac{5\lambda}{4} \quad (4b) \end{cases}$$

for $-\frac{l}{2} < z' < \frac{l}{2}$. In [36], it has been shown that for the normal incidence, the second resonant mode of the dipole can not be excited and so, the induced current around the second mode as (4b) is safely assumed to be zero. In addition, the sinusoidal current assumption is quite valid around the first resonant mode of the dipole as (4a) where I_0 can be obtained in terms of the incident electric field [36]. Obviously based on this assumption, it can be concluded that the scattered field and the Radar Cross Section (RCS) of the short-circuited dipole around its second mode ($\frac{3\lambda}{4} < l < \frac{5\lambda}{4}$) will be zero. Thus, henceforth, all the derivation will be done for only the first mode, and the result for the second mode is correctly supposed to be zero. Considering the dipole as a receiving center-fed dipole antenna which is short-circuited, based on the assumed current distribution (4a), the vector effective length of the dipole can be defined as [37]

$$\vec{l_e}(\theta') = -\frac{\lambda}{\pi}\frac{\cos(\frac{kl}{2}\cos\theta') - \cos(\frac{kl}{2})}{\sin\theta'} \quad (5)$$

and the hypothetical induced open-circuit voltage in the feed point of the dipole can be determined by [37]

$$V_{oc} = \vec{E_i}(\vec{r'}) \cdot \vec{l_e}(\theta') \quad (6)$$

On the other hand, the dipole as a minimum scattering antenna [38] can be modeled by a Thevenin equivalent circuit illustrated in the inset of Fig. 4 [37]. For the sinusoidal current (4a), analytical expressions of the self-impedance ($Z_D{=}R_r + jX_D$) of the dipole have been derived, which are given in [37]. The loss resistance (R_L) of the dipole made from a good conductor is almost negligible. Using the equivalent circuit with the parameters given in [37] for the short-circuit dipole ($Z_L{=}0$), I_0 can be calculated by having the open-circuit voltage. Accordingly, using (5) and (6) with $\theta' = \theta_i = \pi/2$, the amplitude of the induced current on the short-circuited dipole located at ($x'{=}R_0$, $y'{=}0$, $-\frac{l}{2} < z' < \frac{l}{2}$) can be expressed as

$$I_0(t){=}\frac{-\lambda E_0}{\pi Z_D}(1-\cos(\frac{kl}{2}))e^{jkR_0(\cos\phi_i\cos\phi_s+\sin\phi_i\sin\phi_s)} \quad (7)$$

at each rotation angle $\phi_s(t){=}\omega_r t$.

By substituting (7) in (4a) and using the radiation integrals, the quasi-stationary scattered electric field can be calculated based on the induced current. For the normal observation angle of ($\theta_o = \pi/2$, ϕ_o) it can be written as

$$\begin{cases} E^s_\phi(\vec{r},t) = 0 & (8a) \\ E^s_\theta(\vec{r},t) = \frac{-j\lambda E_0\eta e^{-jkr}}{2\pi^2 r Z_D} G_d\ e^{j(\beta_x\cos\phi_s+\beta_y\sin\phi_s)} & (8b) \end{cases}$$

where η is the intrinsic impedance of the background media, $G_d{=}(1-\cos(\frac{kl}{2}))^2$ is the gain factor of the dipole, and $\beta_x{=}kR_0(\cos\phi_i+\cos\phi_o)$ and $\beta_y{=}kR_0(\sin\phi_i+\sin\phi_o)$ are the Doppler phase constants in the x- and y-directions respectively. It should be mentioned that the time-varying phase term in (8b) is the same as the term introduced for rotation-induced micro-Doppler in [39]. To verify (8b), for the special stationary case ($\phi_s(t){=}cte$), we can compare the RCS of the short-circuited dipole calculated using $\sigma{=}\lim_{r\to\infty} 4\pi r^2|\vec{E_s}|^2/|\vec{E_i}|^2$ with the general expression has been given in [40], [41] for the scattering from loaded scatterers as

$$\sigma = \frac{\lambda^2}{\pi}G^2(\theta,\phi)\frac{R_a^2}{|Z_a+Z_L|^2} \quad (9)$$

where Z_L is the load impedance, and $G(\theta,\phi)$, R_a, and Z_a are respectively the gain, the radiation resistance, and the driving-point input impedance of the scatterer if it operates as an antenna. The boresight RCS of the stationary short-circuited dipole can be derived using (8) and (1) when $\phi_s = cte$ as

$$\sigma(f_0) = \frac{\eta^2\lambda^2}{\pi^3}G_d^2\frac{1}{|Z_D|^2} \quad (10)$$

It is worth mentioning that (9) for a short-circuited dipole ($Z_a{=}Z_D, R_a{=}R_r, Z_L{=}0$) with sinusoidal current assumption as (4a), will provide exactly the same expression as (10) for the stationary boresight RCS around the first resonant mode. It can be justified by noting that the expressions given for R_r and $G(\theta = \pi/2,\phi)$ in [35] yielding $R_rG(\theta{=}\pi/2,\phi) = \eta G_d/\pi$ which after substituting in (9) gives an identical expression as (10). In addition, the obtained analytic expression for the stationary RCS in (10) has been verified by simulations done in Ansys HFSS and NEC2 [42], and the results are shown in Fig. 4. Moreover, the validity of the zero-RCS assumption around the second resonant mode has been shown by zero-valued points added to the analytic expression for $\frac{3\lambda}{4} < l < \frac{5\lambda}{4}$ in Fig. 4.

B. Frequency-domain representation of the scattered quasi-stationary field

From mathematical point of view, the expression in (8b) is the complex envelope of the scattered field in real time-domain. The complex envelope is a generalization of the well-known phasor concept while the phasor is restricted to time-invariant amplitude and phase, in contrast to the complex envelope which allows for time-varying parameters [43]. Accordingly, to derive the RCS based on the quasi-stationary fields, the same computations as applied for phasors can be used by obtaining the frequency representation of the complex envelope. Since the rotation is a periodic motion, the resultant quasi-stationary field is a periodic function of the time with the same period as rotation. Thus, (8b) can be

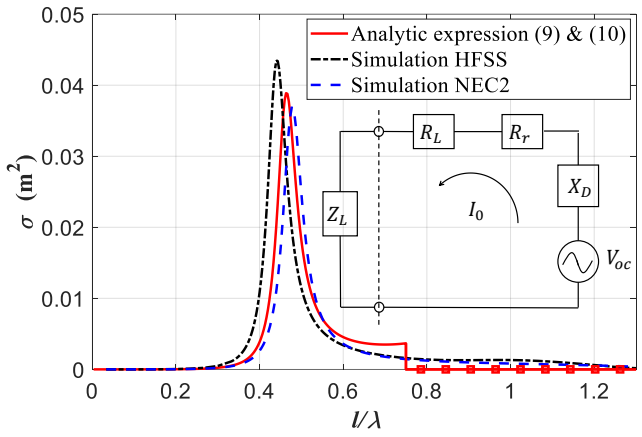

Fig. 4. RCS of the stationary short-circuited dipole with $D = 100\mu m$. The Thevinen equivalent circuit of the dipole is shown in the inset.

represented by a Fourier series with the fundamental frequency of f_r. Without lack of generality, for specular incidence and observation ($\phi_o = \pi - \phi_i$) where β_x=0, the Fourier series coefficients of (8b) can be calculated using the integral representation of the first kind Bessel function of order n as $J_n(x) = \frac{1}{2\pi}\int_{-\pi}^{\pi} e^{j(n\sin\tau - n\tau)}d\tau$ and the resultant Fourier expansion is expressed by [44]

$$E_\theta^s(\vec{r},t) = \frac{-j\lambda E_0\eta e^{-jkr}}{2\pi^2 r Z_D} G_d \sum_{n=-\infty}^{+\infty} J_n(\beta_y) e^{j2n\pi f_r t} \quad (11)$$

By taking the Fourier transform of (11), the spectral representation of the quasi-stationary field can be written as

$$\mathbf{E}_\theta^s(\vec{r},f) = \frac{-j\lambda E_0\eta e^{-jkr}}{2\pi^2 r Z_D} G_d \sum_{n=-\infty}^{+\infty} J_n(\beta_y)\delta(f - nf_r) \quad (12)$$

Also, by taking the Fourier transform of (1), the spectral representation of the incident filed can be written as

$$\vec{\mathbf{E}}_i(\vec{r},f) = E_0\ e^{jk(x\cos\phi_i + y\sin\phi_i)}\delta(f)\ \hat{z} \quad (13)$$

C. Differential RCS of single rotating short-circuited dipole

Differential RCS (or delta-RCS) has been originally introduced for UHF tags which is working based on the back-scattering modulation done by the chip [45]. In [45], the vector differential RCS has been presented including both the amplitude and phase variation of the modulating load in time-domain. Recently, in [46], the differential RCS has been generalized for any modulating tag by using a frequency-domain analysis. According to [46], (12) shows that for the proposed rotating chipless tag, the differential RSC can be associated to the modulated back-scattered power which is located in the non-zero harmonics of the rotation frequency ($nf_r, n \neq 0$) while noting f=0 in (12) corresponds to the carrier frequency of f_0. Thus, the differential RCS for the rotating tag can be defined as

$$\sigma_d(f_0) = \lim_{r\to\infty} 4\pi r^2 \times \frac{\int_{-\infty}^{-\epsilon} |\mathbf{E}_\theta^s(\vec{r},f)|^2\, df + \int_{+\epsilon}^{+\infty} |\mathbf{E}_\theta^s(\vec{r},f)|^2\, df}{\int_{-\infty}^{+\infty} |\vec{\mathbf{E}}_i(\vec{r},f)|^2\, df} \quad (14)$$

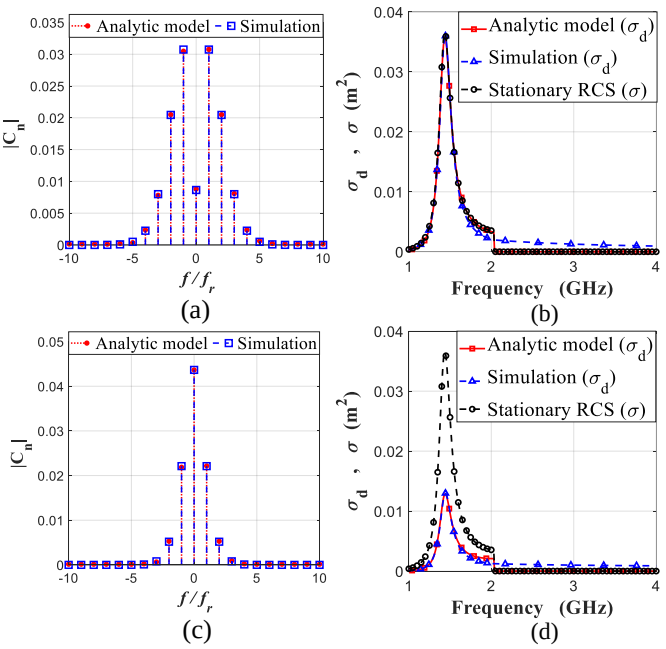

Fig. 5. Calculated Fourier coefficients of the quasi-stationary scattered field from a rotating dipole with l=100 mm and D=100 μm at its first resonance frequency (1.47 GHz) (a) for R_0=35 mm and (c) for R_0=15 mm. Calculated differential RCS of the rotating dipole (b) for R_0=35 mm and (d) for R_0=15 mm. Calculations have been done based on the analytic model and simulations in NEC2.

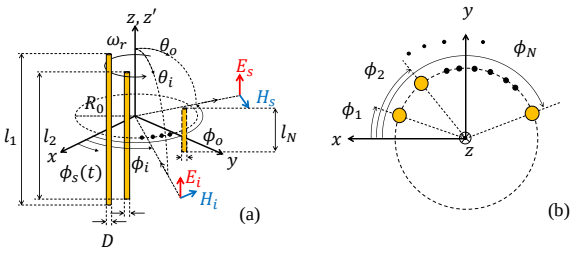

Fig. 6. N short-circuited simultaneously rotating dipoles with the lengths of $l_1, l_2, ..., l_N$ normally impinged by a time-harmonic linearly z-polarized plane wave. All the dipoles have the same diameter of D. (a) 3D view. (b) Top view.

where ϵ is an infinitesimal small positive number. By substituting (12) and (13) in (14) and using the well-known equality of $\sum_{n=-\infty}^{+\infty} |J_n(x)|^2 = 1$, (14) can be simplified as

$$\sigma_d(f_0) = \sigma(f_0)[1 - J_0^2(\beta_y)] \quad (15)$$

which nicely relates the differential RCS obtained from the quasi-stationary back-scattered field to the classical stationary RCS of the short-circuited dipole $\sigma(f_0)$. Although (15) has been derived for the short-circuited dipole scatterer, energy conservation law and orthonormal property of the Bessel harmonics guarantee that the differential RCS of any single rotating scatterer can be expressed same as (15). Equation (15) shows that β_y=$kR_0(\sin\phi_i + \sin\phi_o)$ is the key parameter which determines the maximum achievable differential RCS for the rotating dipole. Without lacking generality, in the monostatic configuration with ϕ_i=ϕ_o=$\pi/2$, the Doppler phase constant is simplified to β_y=$2kR_0$ which clearly indicates

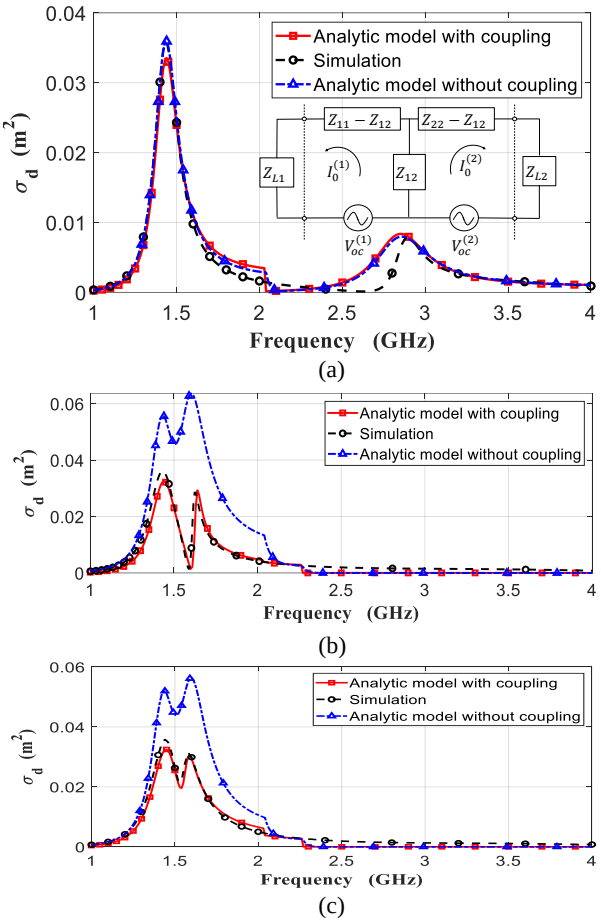

Fig. 7. Calculated differential RCS of the two dipoles with D=100 μm rotating at the radius of R_0=35 mm (a) for l_1=100 mm, l_2=50 mm, and ϕ_d=5°, (b) for l_1=100 mm, l_2=90 mm, and ϕ_d=5°, and (c) for l_1=100 mm, l_2=90 mm, and ϕ_d=30°. The equivalent circuit for two coupled dipoles is shown in the inset of (a). Calculations have been done based on the analytic model and simulations in NEC2.

that the radius of the rotation should be properly chosen to maximize the differential RCS at the resonance frequency of the dipole. By computing the zeros of $J_0(x)$, the first optimum value for β_y is obtained as 2.41. For a 100 mm length rotating dipole, Fig. 5(a) and (c) illustrate the Fourier coefficients (C_n) of the quasi-stationary scattered field at the resonance frequency when R_0=35 mm (β_y=2.12) and R_0=15 mm (β_y=0.905) respectively. Obviously, for R_0=35 mm the scattered power is mostly modulated into the higher order Bessel harmonics (n>0) whereas for R_0=15 mm the scattered power is almost concentrated in the zeroth harmonic not contributing in the differential RCS. Consequently, as it is shown in Fig. 5(b) and (d), for R_0=35 mm the differential RCS almost has reached its maximum value [$\sigma(f_0)$] corresponds to β_y=2.41 while for R_0=15 mm it has been reduced significantly at the resonance.

D. Scattering from N rotating short-circuited dipoles

Previously presented demonstration can be generalized to obtain the scattered field from N rotating short-circuited dipoles with the lengths of $l_1, l_2, ..., l_N$ in decreasing order which are located in the same radius of R_0 and different azimuth angles of $\phi_1, \phi_2, ..., \phi_N$ respectively, as shown in Fig. 6. All the dipoles are aligned with the z-axis and impinged by a normal incident ($\theta_i = \pi/2, \phi_i$) z-polarized electric field. Also, all dipoles are rotated simultaneously with $\phi_s(t) = \omega_r t$ around the z-axis. The length of the shortest and the longest dipoles are chosen such that $l_N \geq 2l_1/5$ making the current distribution in (4) valid for all dipoles at the desiered frequency range of $\lambda \geq \frac{4}{5} l_1$. In other words, this choice guarantees the third resonance frequency of the longest dipole is sufficiently higher than the first resonance frequency of the shortest dipole. Thus, with a similar approach, the hypothetical induced voltage on the n-th dipole (while all dipoles are open-circuited) can be expressed as

$$V_{oc}^{(n)} = \vec{E}_i(\vec{r_n}) \cdot \vec{l}_e^{\,n}(\theta' = \pi/2) \quad n = 1, ..., N \qquad (16)$$

where $\vec{l}_e^{\,n}(\theta)$ is the vector effective length of the n-th dipole and $\vec{E}_i(\vec{r_n})$ is the incident electric filed calculated in the position of the n-th dipole using the corresponding rotation transformation of $[r] = [R_t(\phi_s(t) + \phi_n)][r'_n]$ which is applied to (1). It is noteworthy to mention that in (16) the induced open-circuit voltage on each dipole is assumed to be only due to the incident wave and not affected by the scattered field from the other existing open-circuited dipoles. This assumption is allthemore valid since the dipole, as a minimum scattering antenna, will not provide any scattering when it is open-circuited [38]. Using the impedance matrix representation for N dipoles as an N-port network, the induced current on each dipole can be obtained while the coupling effect is taken into account. Accordingly, the induced current on each short-circuited dipole can be derived in terms of the open-circuit voltages as

$$\begin{bmatrix} I_0^{(1)} \\ \vdots \\ I_0^{(N)} \end{bmatrix} = \begin{bmatrix} Z_{11} & \cdots & Z_{1N} \\ \vdots & Z_{nm} & \vdots \\ Z_{N1} & \cdots & Z_{NN} \end{bmatrix}^{-1} \begin{bmatrix} V_{oc}^{(1)} \\ \vdots \\ V_{oc}^{(N)} \end{bmatrix} \qquad (17)$$

where Z_{nn} is the self-impedance of the n-th dipole and $Z_{nm\ (n\neq m)}$ is the mutual impedance between the n-th and m-th dipole which has been given in [37] for sinusoidal current distributions. However, for the generalized case of N rotating coupled dipoles, zero-current assumption at the second resonant mode (4b) can not be just applied to $I_0^{(n)}$ $n = 1, ..., N$ at the last step of the calculation process as it was done for the single dipole. Considering the coupling, the calculation process is involved with a Z-matrix inversion. As the given expressions for self and mutual terms in [37] has been generally derived without zero-current assumption at the second resonance, some spurious solutions will be produced during the Z-matrix inversion in our case. To avoid these spurious solutions, it is necessary to modify the given expressions for impedance terms in [37]. For the simplest case of $N = 2$, the equivalent circuit of the two coupled dipoles is shown in the inset of the Fig. (7). According to this equivalent circuit, for two short-circuited dipole, when $3\lambda/4 < l_1 < 5\lambda/4$ and $l_2 < 3\lambda/4$, the zero induced current on the first dipole will be obtained if we assume Z_{11}=∞ and Z_{21}=Z_{12}=0. This can be

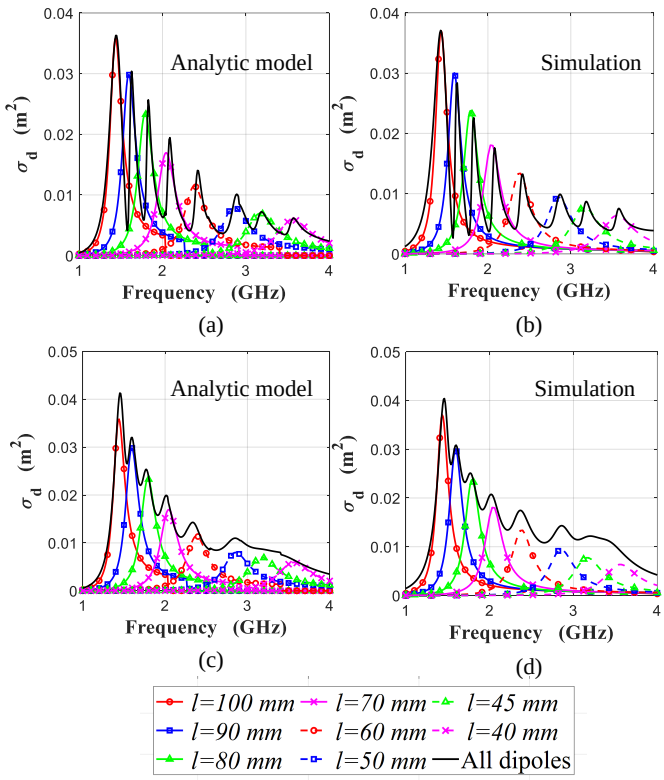

Fig. 8. Calculated differential RCS of the 8 dipoles with the lengths of l_1=40 mm, l_2=50 mm,$\cdots$, l_8=100 mm and D=100 μm rotating at the radius of R_0=35 mm for each single dipole and when all dipoles are present, based on (a) analytic model and (b) simulation with ϕ_d=5°, and (c) analytic model and (d) simulation with ϕ_d=30°.

generalized to N dipoles by applying the following conditions to the self and mutual impedance terms.

$$\begin{cases} Z_{nn}=\infty & \dfrac{3\lambda}{4}<l_n<\dfrac{5\lambda}{4} \quad (18a) \\ Z_{nm}{=}Z_{mn}{=}0 \quad (n\neq m) & \dfrac{3\lambda}{4}<l_n \text{ or } l_m<\dfrac{5\lambda}{4} \quad (18b) \end{cases}$$

It should be clarified that applying (18) to Z-matrix elements is sufficient to correctly compute the induced currents and no more constraints is needed to be applied in the calculation process. By calculating the currents, based on the superposition theorem, the total quasi-stationary scattered field components at the normal observation angle of $(\theta_o = \pi/2, \phi_o)$ can be written as

$$E^t_{s\theta}(\vec{r},t){=}\sum_{n=1}^{N}\frac{j\eta I_0^{(n)}e^{-jkr}}{2\pi r}(1-\cos(\frac{kl_n}{2})) \times e^{jkR_0(\cos\phi_o\cos(\phi_s+\phi_n)+\sin\phi_o\sin(\phi_s+\phi_n))} \quad (19)$$

and $E^t_{s\phi}(\vec{r},t){=}0$. Although (19) is a periodic function with the fundamental frequency of f_r, its Fourier series coefficients can not be analytically expressed like (11) anymore. However, the differential RCS for N rotating dipoles can be obtained using (14) by calculating the Fourier series coefficients of (19) and then its frequency representation. For the sake of simplicity, dipoles are supposed to be equispaced as $\phi_n{=}n\phi_d$, $n{=}1,...,N$ where ϕ_d is the azimuth angle between each two adjacent dipoles. To show the validity of

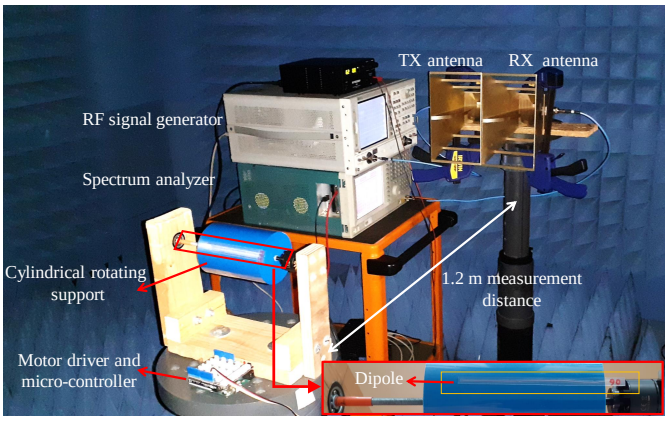

Fig. 9. Measurement bench used for identification of the rotating chipless tags.

the assumptions introduced in (18), the differential RCS of the two rotating dipoles is studied while their lengths are chosen such that the first resonance of the shorter dipole is exactly coincided with the second resonance of the longer one. For l_1=100 mm and l_2=50 mm, Fig. 7(a) shows the calculated differential RCS using the analytical model and simulation. The good agreement between the results obtained from the model and the simulation verifies the assumption has been proposed for the self and mutual terms in (18). In the proposed analytic model, the coupling effect between the dipoles has been included to accurately predict the differential RCS. However, this model can be easily simplified to a special case in which the coupling effect is ignored by putting all the mutual terms (Z_{nm}; $n \neq m$) equal to zero. A comparison between the results obtained from the analytic model with and without the coupling will show the importance of including the mutual terms. Based on the simplified model the induced currents can be obtained by

$$I_0^{(n)}=\frac{V_{oc}^{(n)}}{Z_{nn}} \quad n=1,...,N \quad (20)$$

which after substituting in (19) yields the scattered field. Actually, in the simplified model, the rotating dipoles will be considered as a reflect-array in which the phase and the amplitude of the induced current on each element is defined by (16) and (20). For two rotating dipoles with the lengths of l_1=100 mm and l_2=50mm, as it can be observed in Fig. 7(a), the differential RCS calculated using the simplified model is almost the same as those has been calculated based on the model with coupling. But it should be noted that in this case, actually, the first resonance of the dipoles are completely separated which making the coupling effect negligible. However, for two rotating dipoles with close together lengths of l_1=100 mm and l_2=90 mm the situation is totally different. For the two closely resonant dipoles, Fig. 7(b) and (c) show the calculated differential RCS based on the analytic model with and without coupling, and compare them with simulation based results. It can be observed that the simplified model can not predict well the differential RCS for neither strongly coupled dipoles [ϕ_d=5°, Fig. 7(b)] nor weakly coupled dipoles [ϕ_d=30°, Fig. 7(c)] which clearly proves the necessity of

TABLE I
MEASURED HARMONIC AMPLITUDE RATIO AND CORRESPONDING BESSEL HARMONICS RATIO

Measured harmonic ratio (dB)		Bessel harmonic ratio (dB)	
$A_2 - A_1$	-6.16	J_2/J_1	-4.31
$A_3 - A_1$	-15.41	J_3/J_1	-13.08
$A_4 - A_1$	-27.12	J_4/J_1	-24.69

the including mutual coupling. Finally, the validity of the proposed analytic model has been examined for eight dipoles with the lengths of $40, 50, ..., 100$ mm in the both strongly coupled (ϕ_d=5°) and weakly coupled (ϕ_d=30°) cases which are shown in Fig. 8(a) and (c) respectively. Corresponding simulation results are illustrated in Fig. 8(b) and (d) which are quite compatible with the analytic results obtained for the differential RCS.

IV. Results and Discussion

A. Measurement bench

Fig. 9 presents the measurement bench composed of a Vector Network Analyzer (VNA) (HP 8720D) and a Spectrum Analyzer (SA) (Tektronix RSA3408A) which are connected to the transmitting and receiving antennas (A.H. Systems, INC. SAS-571) respectively. Note that the VNA operates in CW mode and only acts as an RF source to generate the stepped-frequency CW signal. Coherent transmission-reception process is a well-known concept in micro-Doppler radars which is necessary in order to preserve small phase variations induced by low-speed motions [20]. Accordingly, in this work also, both instruments (VNA and SA) are synchronized using the same 10 MHz reference signal to provide an accurate measurement procedure. To realize the rotational motion perfectly fitted to the proposed model, dipoles will be mounted on a rotating dielectric cylinder driven by a motor. As it was mentioned in Section II, a cylinder rotating around its axis, due to its perfect revolutional symmetry, can not produce any motion-induced time variation and acts same as other stationary objects present in the background. Thus, this cylindrical support can be safely utilized for the measurement process. A simple wooden stand has been fabricated and used to correctly assemble the cylinder and the motor. The dielectric cylinder has been realized through a standard 3D printing process to provide a fully-symmetric cylinder with a defined radius. The optimum radius for the cylinder has been determined using (15) as 35 mm for dipoles resonating between $1-4$ GHz. The TX and RX antennas have been placed in close proximity, and aligned vertically with the rotating support to realize the monostatic configuration compatible with the model. Moreover, the rotating support is placed at a distance of d=1.2 m from the antennas to fulfill the far-field radiation condition. The transmission frequency (f_0) can be set in-between 1 and 4 GHz with the desired step and the output power (P_t) has been set to 0 dBm. The spectrum analyzer in FFT mode acquires the received signal over a span of 250 Hz around each CW signal generated by the VNA. The short-circuited dipole scatterers with defined lengths have been designed using a

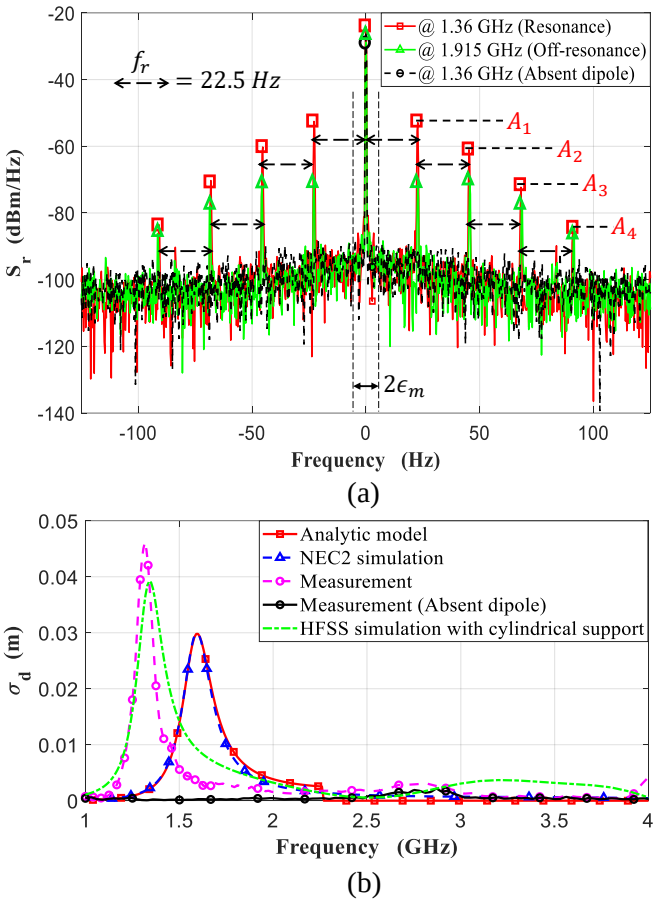

Fig. 10. (a) Measurement of the backscattered PSD for the 90 mm length rotating dipole at two carriers associated to resonance and off-resonance frequencies. Absent dipole corresponds to the PSD of the background when cylindrical support is still rotating while the dipole has been removed. (b) Calculated differential RCS of the 90 mm length rotating dipole based on the measured PSD, analytic model, and simulations done in NEC2 and HFSS.

100 μm copper wire. To increase the mechanical robustness of the dipoles, they have been encapsulated in-between two layers of PET sheets. As it is shown in the inset of Fig. 9, the designed dipole scatterers can be mounted on the cylindrical support which is rotated by the motor with a frequency of 22.5 turns/sec. The entire setup is located in the anechoic chamber and can be controlled by a remote computer from outside.

B. Single rotating dipole

Using the described measurement bench, the Power Spectral Density (PSD) of the back-scattered signal from a 90 mm length rotating short-circuited dipole has been measured at 30 MHz-stepped CWs between 1 and 4 GHz. For two carrier frequencies, the down-converted measured PSD $S_r(f)$ which is associated to the complex envelope of the quasi-stationary back-scattered field are shown in Fig. 10(a). As predicted by (12), the frequency components generated due to the rotation can be clearly observed at nf_r=$n \times$ 22.5 Hz. In addition, the measured PSD for when the dipole is not mounted on the rotating support has been shown in Fig. 10(a). Obviously, as it was expected, by removing the dipole scatterer, the

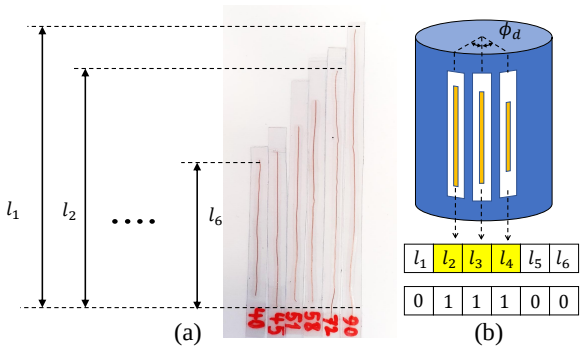

Fig. 11. (a) Fabricated short-circuited dipole scatterers. (b) Mounted dipole scatteres on the cylindrical support to form the chipless tag and its assigned ID. Dipoles are mounted such that $\phi_d \approx 5^\circ$.

background response has only a single frequency component located at f=0 which is exactly associated to the transmission frequency of f_0.

Differential RCS of the rotating dipole can be calculated based on the measured PSD at each f_0. Similarly to (14), the modulated back-scattered power (P_{bsd}) which is associated to the components located around $f = 0$ can be obtained using

$$P_{bs\,d} = \int_{-\infty}^{-\epsilon_m} S_r(f)\,df + \int_{+\epsilon_m}^{+\infty} S_r(f)\,df \qquad (21)$$

where $2\epsilon_m$ is the minimal bandwidth which allows to remove the power at $f = 0$. Using the well-known radar equation [37], differential RCS of the rotating dipole at f_0 can be calculated as

$$\sigma_d(f_0) = \frac{(4\pi)^3 d^4 P_{bs\,d}}{\lambda^2 G_r G_t (1-|\Gamma_r|^2)(1-|\Gamma_t|^2) P_t} \qquad (22)$$

where G_r, Γ_r and G_t, Γ_t are the gain and the input reflection coefficient of the receiving and transmitting antennas respectively which are given in [47]. The calculated differential RCS of the rotating dipole based on (21) and (22) is presented in Fig. 10(b). In addition, it has been compared with the calculated differential RCS of a 90 mm length dipole rotating at the radius of 35 mm based on the analytic model and simulation. Due to the dielectric constant of the cylindrical support ($\epsilon_r \approx 1.4$), the measured resonance frequency of the dipole (1.36 GHz) has been shifted down compare to that is obtained by the model and NEC2 simulation in both of which the dipole is assumed in free space. This frequency shift can be easily justified by doing a full-wave HFSS simulation to compute the RCS of the dipole when it is mounted on the dielectric cylinder. Using the RCS obtained from HFSS and (15), the calculated differential RCS has been shown in Fig. 10(b) which is in good agreement with measurement result and verifies the proposed model. Moreover, at the resonance frequency for example, the amplitude ratio of the frequency components at nf_r shown in Fig. 10(a) are compared with the corresponding Bessel harmonics ratio in Table I. The Bessel harmonics ratio for β_y=1.99 associated to the resonance frequency, is compatible with the measurement results in term of the relative succession for harmonics.

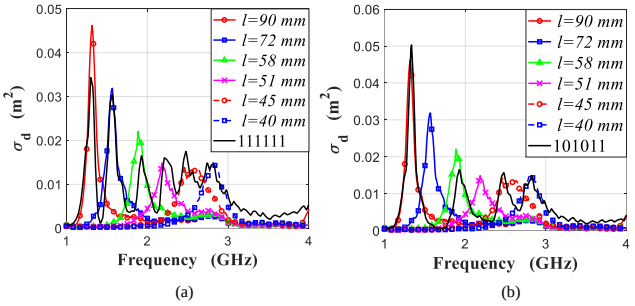

Fig. 12. Differential RCS of the 6 fabricated dipoles superimposed by the differential RCS of (a) "111111" tag and (b) "101011" tag, as a function of f_0. Differential RCS has been calculated based on the measured PSD

C. Tag design and identification

The previously presented results in Fig. 8 for differential RCS of $N = 8$ rotating dipoles calculated based on the model can be utilized to design a rotating chipless tag. In classical frequency-coded chipless tags, the ID data is associated to the resonance peaks observed in the measured RCS of the tag. Similarly, as it is obvious in Fig. 8, differential RCS of N rotating dipole scatterers with different lengths, can be considered as an identification function which data is coded in it with presence or absence of a given resonator. In addition, to provide an easy identification process, differentiable resonance peaks are desired in the differential RCS response. Thus, tags consist of closely positioned rotating dipoles (strongly coupled) are proposed to be fabricated and measured here. Of course, the radius of rotation is an important parameter and should be chosen optimally to maximize differential RCS in the desired frequency band. As it was described in the measurement bench, the optimum radius of $R_0 = 35$ mm has been designed here for dipoles resonating between 1 and 4 GHz.

Six short-circuited dipoles with the lengths of l_1=90 mm, l_2=72 mm, l_3=58 mm, l_4=51 mm, l_5=45 mm, and l_6=40 mm have been fabricated using the process explained before and shown in Fig. 11(a). As it is illustrated by Fig. 11(b), the fabricated dipoles have been employed to implement tags with different IDs by mounting the selected dipoles on the cylinder where the azimuth angle in between them has been set to $\phi_d \approx 5^\circ$. Differential RCS of the single dipoles have been calculated based on the measured PSD and presented as a function of carrier frequency (f_0) in Fig. 12. The measured differential RCS of the two designed tags with IDs of "111111" and "101011" are superimposed on the measured differential RCS of the single dipoles in Fig. 12(a) and (b) respectively. For both tag IDs, clearly separated peaks at the resonance frequencies of the dipoles which are present in the tag, demonstrate the identification process with a coding capacity of 6 bits. However, the maximum achievable coding capacity for the multi-dipole tag can be estimated by dividing the total available bandwidth (2.9 GHz) by the 3dB-bandwidth of a single dipole (350 MHz). Thus, as it has been shown by the model (Fig. 8), in the proof of concept, the coding capacity of the proposed multi-dipole tag can be increased up to 8 bits in the bandwidth of 1 to 3.9 GHz.

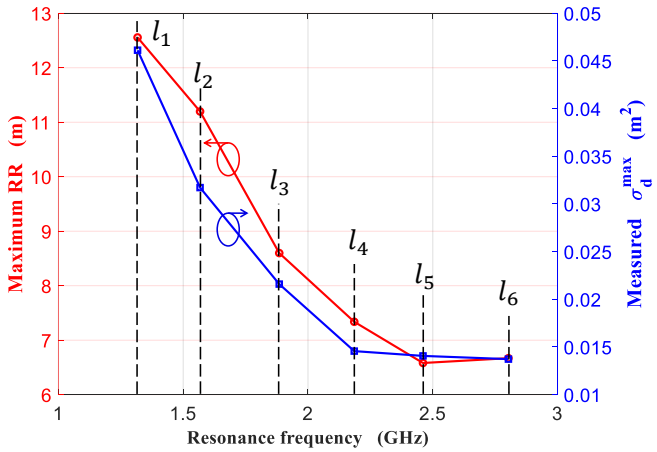

Fig. 13. Calculated maximum read range and the maximum measured differential RCS of the 6 used dipoles as a function of their resonance frequencies. Maximum read range is calculated for P_t=5 dBm and $P_{r\,min}$= − 85 dBm.

D. Read range

Read range is one the most critical challenges in the context of chipless RFID on which this paper is focused. The main proposed idea to increase the read range which has been explained schematically in Section II, can be perfectly verified in measurement based on the results shown in Fig. 10(a). Observing the measured PSD of the back-scattered signal at f=0 (corresponds to the carrier frequency) for the three cases illustrated in Fig. 10(a) as "Resonance", "Off-resonance", and "Absent dipole", indicates that the dynamic variation of the received signal for the three cases is less than 5 dB. This clarifies the non-desired effect of the LTI property which limits the read range for stationary chipless tags. On the other hand, by doing the same observation at nf_r, the dynamic variation of the rotation induced harmonics in the three cases is more than 40 dB which obviously provides detection at larger distances compared to the stationary case. Accordingly, time-varying property of the motion can be practically utilized to increase the reading range of the chipless tags significantly.

For a given transmitted power (P_t) and receiver sensitivity ($P_{r\,min}$), the maximum reading range (RR) of each fabricated dipole can be calculated based on the maximum measured differential RCS at the resonance frequency (σ_d^{max}) using

$$RR^{max} = \sqrt[4]{\frac{\lambda^2 G_r G_t (1-|\Gamma_r|^2)(1-|\Gamma_t|^2) P_t \sigma_d^{max}}{(4\pi)^3 P_{r\,min}}} \quad (23)$$

where the antenna parameters G_t, G_r, Γ_t, and Γ_r has been previously addressed for the present measurement bench . The resonance frequency and its associated maximum differential RCS for each single dipole can be extracted from the measurement results presented in Fig. 12. For P_t=5 dBm and $P_{r\,min}$= − 85 dBm, the calculated maximum reading range of the six fabricated dipoles and their maximum differential RCS are shown in Fig. 13 versus the resonance frequencies. The results in Fig. 13 clearly demonstrate that read range of at least 6 m is achievable for all the dipole resonators in an isolated environment like anechoic chamber.

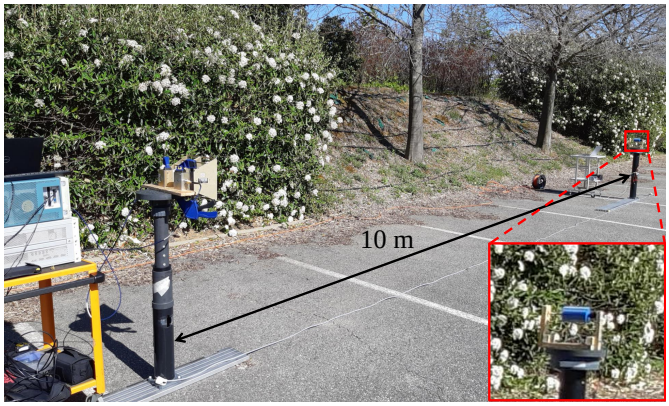

Fig. 14. Measurement setup used to experimentally study the read range in a real environment.

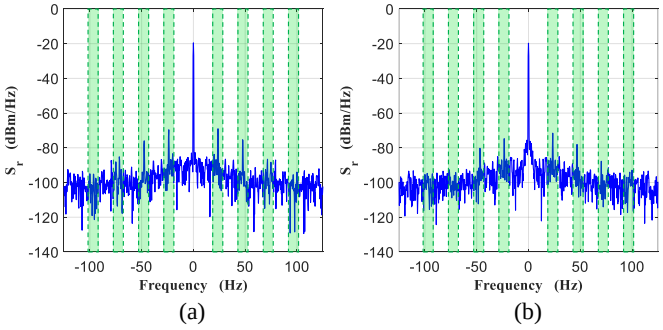

Fig. 15. Measured back-scattered PSD for 90 mm length rotating dipole at the distance of (a) 4 m and (b) 8 m in the real environment (see Fig. 14). The carrier frequency has been set to 1.36 GHz and the dipole has been rotated at f_r=22.5 Hz. The utilized filter mask in the post-processing is shown by green highlighted bars.

Finally, to verify the maximum read range experimentally, the 90 mm length dipole has been examined with the setup shown in Fig. 14 in a real environment. The same instruments (VNA and SA) have been used, and the TX-RX antennas are aligned with the rotating support using a LASER level. Dipole is rotating at 22.5 Hz and the carrier frequency has been set at the resonance frequency of the dipole (1.36 GHz) while the output power is 5 dBm. The modulated back-scattered power from rotating dipole has been measured at the distance of 1 to 10 m with a 20 cm step. Fig. 15(a) and (b) illustrate the measured PSD at the distance of 4 m and 8 m respectively. Obviously, the rotation induced harmonics can be easily detected for 8 m range which implies that the tag is readable at even larger distances. To calculate $P_{bs\,d}$ at each distance based on the measured PSD, a filter mask has been used as it is shown in Fig. 15. Actually, in the real environment, using (21) to compute $P_{bs\,d}$ will pass some errors into the results which is caused by the fluctuations exist in the acquired bandwidth. As we know the rotation frequency, the filter mask can be accurately designed and applied in the post-processing to remove the non-desired in-band fluctuations. Utilizing the introduced mask, the measured $P_{bs\,d}$ as a function of distance is depicted in Fig. 16. In addition, by having the measured σ_d^{max} of the dipole, the modulated back-scattered power can be theoretically computed using (22) which is

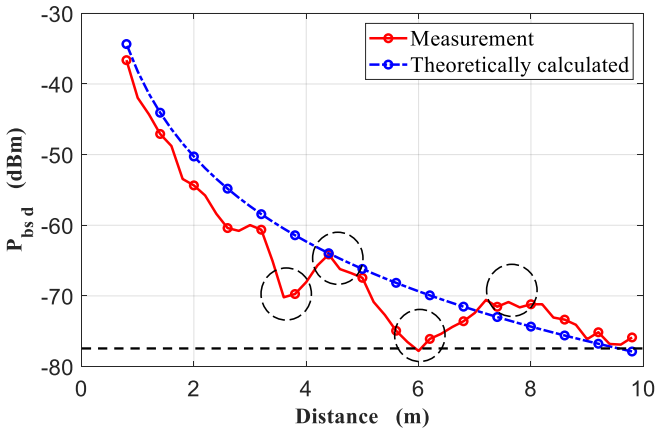

Fig. 16. Measured and theoretically calculated $P_{bs\,d}$ (modulated back-scattered power) as a function of distance in a real environment (see Fig. 14).

shown in Fig. 16. The overall decreasing behaviour of the measured $P_{bs\,d}$ as a function of distance is compatible with the theoretical result. However, for $d > 3$ m, some local maximum and minimums can be observed for the measured power which are indicated by dashed circles in Fig. 16. This phenomenon can be justified by the effect of ground reflection which caused constructive and destructive interference in the maximum and minimum regions respectively. Accordingly, the absolute maximum read range can not be easily determined in the real environment. But of course, by introducing a new threshold linked to the minimum measured power, as it is depicted by a dashed line in Fig. 16, the intersection point between theoretically calculated $P_{bs\,d}$ and the threshold line will give the maximum achievable read range in real environment as 9.6 m. Note that the maximum read range of a tag consisting several dipoles, will be determined by the smallest dipole. According to read range results obtained for 90 mm length dipole in real environment and the theoretically studied read range in Fig. 13, tags including the smallest dipole with the length of l_6, as the worst case, are still readable at distances up to 3 m which outperform the ones associated to classical chipless tag detection by a factor of 10. Furthermore, this performance can be increased simply by increasing the transmission power (P_t) or the antennas gain (G_r, G_t).

E. Perspectives

Although the rotational motion has been considered through this paper, the introduced concept is applicable for other common movements like translation and vibration. From a theoretical point of view, the presented subject can be incorporated in any identification and sensing applications in which the tagged target is moving. But of course, in practical situations the detection process will be faced with some challenges due to the micro-Doppler generated by the other existing moving objects in the environment, specially the tagged object itself. However, these challenges can be resolved using efficient detection methods (some of these techniques have already been introduced for classical chipless tags such as cross-polarization readings and can be directly taken for the case of moving tags) and tag design for specific applications. Accordingly, all the applications which have been already proposed based on micro-Doppler effect can be considered to be incorporated with chipless RFID based on the introduced concept. In the following, we have tried to mention several key examples based on the three common motions as rotation, vibration, and translation. In case of rotation, chipless tags can be attached to plastic propellers of a quadcopter providing identification of the drone when it is flying. Also, this scenario can be applied for rotating arms of an anemometer to realized a remote wind speed sensing. For vibration case, there are a lot of applications in structural and human health monitoring which are involved with very low-frequency micro-Doppler generated by slowly vibrating parts. Chipless tags mounted on these moving parts can be used to identify specific parts of the structure or human body and to detect probable critical situations in each part remotely. Finally, in case of translation, for tagged object carried by a conveyor belt which are the most common example in RFID context, the Doppler component - instead of micro-Doppler components - can be utilized to detect a chipless tag from larger distances. It should be mentioned that in case of translation, the amplitude of the back-scattered signal, as well as its phase, will vary during the detection and should be considered in practice.

V. Conclusion

We proposed identification and read range enhancement of chipless tags exploiting the micro-Doppler effect for the first time. To predict back-scattering behaviour of the moving chipless tag, a model has been developed based on equivalent circuit of the single and coupled short-circuited dipole scatterers. The differential RCS of the tag has been calculated analytically and measured. The measurement results are in accordance with the theory, and experimentally verifies the identification process. Read range of the rotating chipless tag has been measured in real environment which shows that reading distances of several meters can be achieved. A rotational movement of the tag was studied for ease of implementation. However, the approach is not limited to this type of movement and this principle can be used on tags moving at a lower speed. To detect low-frequency micro-Doppler induced by slow movements, any simple portable reader can be used provided that the transmitter and receiver use a single local oscillator for coherent reception. Last but not least, extremely simple resonators were considered in the study to demonstrate the principle from both a theoretical and a practical point of view. Much better resonators (with higher quality factors as well as higher RCS) are commonly used in RFID chipless and can be directly used in the same way, thus increasing both the coding capacity and the reading distance.

Acknowledgment

This work was supported by the European Research Council (ERC) through the European Union's Horizon 2020 Research and Innovation Program (ScattererID) under Grant N° 772539.

REFERENCES

[1] M. A. Islam and N. C. Karmakar, "A novel compact printable dual-polarized chipless RFID system," *IEEE Trans. Microw. Theory Tech.*, vol. 60, no. 7, pp. 2142–2151, 2012.

[2] A. Vena, E. Perret, S. Tedjini, G. Eymin Petot Tourtollet, A. Delattre, F. Garet, and Y. Boutant, "Design of chipless RFID tags printed on paper by flexography," *IEEE Trans. Antennas Propag.*, vol. 61, no. 12, pp. 5868–5877, 2013.

[3] S. K. Behera and N. C. Karmakar, "Chipless RFID printing technologies: A state of the art," *IEEE Microw. Mag.*, vol. 22, no. 6, pp. 64–81, 2021.

[4] A. Vena, E. Perret, and S. Tedjini, "Chipless RFID tag using hybrid coding technique," *IEEE Trans. Microw. Theory Tech.*, vol. 59, no. 12, pp. 3356–3364, 2011.

[5] F. Costa, S. Genovesi, and A. Monorchio, "A chipless RFID based on multiresonant high-impedance surfaces," *IEEE Trans. Microw. Theory Tech.*, vol. 61, no. 1, pp. 146–153, 2013.

[6] A. Vena, E. Perret, and S. Tedjini, "High-capacity chipless RFID tag insensitive to the polarization," *IEEE Trans. Antennas Propag.*, vol. 60, no. 10, pp. 4509–4515, 2012.

[7] M. Khaliel, A. El-Awamry, A. Fawky Megahed, and T. Kaiser, "A novel design approach for co/cross-polarizing chipless RFID tags of high coding capacity," *IEEE J. Radio Freq. Identif.*, vol. 1, no. 2, pp. 135–143, 2017.

[8] F. Babaeian and N. C. Karmakar, "Development of cross-polar orientation-insensitive chipless RFID tags," *IEEE Trans. Antennas Propag.*, vol. 68, no. 7, pp. 5159–5170, 2020.

[9] A. Vena, E. Perret, and S. Tedjini, "Design of compact and auto-compensated single-layer chipless RFID tag," *IEEE Trans. Microw. Theory Tech.*, vol. 60, no. 9, pp. 2913–2924, 2012.

[10] A. Vena, E. Perret, D. Kaddour, and T. Baron, "Toward a reliable chipless RFID humidity sensor tag based on silicon nanowires," *IEEE Trans. Microw. Theory Tech.*, vol. 64, no. 9, pp. 2977–2985, 2016.

[11] C. Herrojo, J. Mata-Contreras, F. Paredes, and F. Martín, "Microwave encoders for chipless RFID and angular velocity sensors based on S-shaped split ring resonators," *IEEE Sensors J.*, vol. 17, no. 15, pp. 4805–4813, 2017.

[12] F. Costa, A. Gentile, S. Genovesi, L. Buoncristiani, A. Lazaro, R. Villarino, and D. Girbau, "A depolarizing chipless RF label for dielectric permittivity sensing," *IEEE Microw. Wireless Compon. Lett.*, vol. 28, no. 5, pp. 371–373, 2018.

[13] A. M. J. Marindra and G. Y. Tian, "Chipless RFID sensor tag for metal crack detection and characterization," *IEEE Trans. Microw. Theory Tech.*, vol. 66, no. 5, pp. 2452–2462, 2018.

[14] M. A. Islam and N. C. Karmakar, "An 8×8 mm-wave LP ACMPA array for a long-range mm-wave chipless RFID tag-sensor reader," *IEEE J. Radio Freq. Identif.*, vol. 5, no. 1, pp. 53–63, 2021.

[15] R. Koswatta and N. Karmakar, "Investigation into antenna performance on read range improvement of chipless RFID tag reader," in *2010 Asia-Pacific Microwave Conference Proceedings (APMC)*, Yokohama, Japan, Dec. 2010, pp. 1300–1303.

[16] M. Khaliel, A. El-Awamry, A. Fawky, and T. Kaiser, "Long reading range chipless RFID system based on reflectarray antennas," in *2017 11th European Conference on Antennas and Propagation (EuCAP)*, Paris, France, Mar. 2017, pp. 3384–3388.

[17] N. Barbot, O. Rance, and E. Perret, "Classical RFID versus chipless RFID read range: Is linearity a friend or a foe?" *IEEE Trans. Microw. Theory Tech.*, 2021, early access.

[18] B. Colpitts and G. Boiteau, "Harmonic radar transceiver design: miniature tags for insect tracking," *IEEE Trans. Antennas Propag.*, vol. 52, no. 11, pp. 2825–2832, 2004.

[19] X. Gu, N. N. Srinaga, L. Guo, S. Hemour, and K. Wu, "Diplexer-based fully passive harmonic transponder for sub-6-GHz 5G-compatible IoT applications," *IEEE Trans. Microw. Theory Tech.*, vol. 67, no. 5, pp. 1675–1687, 2019.

[20] V. C. Chen, *The micro-Doppler effect in radar*. Artech House, 2019.

[21] A. Lazaro, M. Lazaro, R. Villarino, and P. De Paco, "New radar micro-Doppler tag for road safety based on the signature of rotating backscatters," *IEEE Sensors J.*, vol. 21, no. 6, pp. 8604–8612, Mar. 2021.

[22] N. Barbot and E. Perret, "Linear time-variant chipless RFID sensor," *IEEE Journal of Radio Frequency Identification*, submitted.

[23] V. Chen, W. Miceli, and D. Tahmoush, *Radar Micro-Doppler Signatures: Processing and Applications*. Institution of Engineering and Technology, 2014.

[24] B. K. Kim, H.-S. Kang, and S.-O. Park, "Drone classification using convolutional neural networks with merged Doppler images," *IEEE Geosci. Remote Sens. Lett.*, vol. 14, no. 1, pp. 38–42, 2016.

[25] Y. Sun *et al.*, "Micro-Doppler signature-based detection, classification, and localization of small UAV with long short-term memory neural network," *IEEE Trans. Geosci. Remote Sens.*, 2020.

[26] A. Madanayake *et al.*, "Physics-aware processing of rotational micro-Doppler signatures for DBN-based UAS classification radar," in *2020 IEEE International Conference on RFID*, 2020, pp. 1–8.

[27] Y. Kim and H. Ling, "Human activity classification based on micro-Doppler signatures using a support vector machine," *IEEE Trans. Geosci. Remote Sens.*, vol. 47, no. 5, pp. 1328–1337, 2009.

[28] D. P. Fairchild and R. M. Narayanan, "Classification of human motions using empirical mode decomposition of human micro-Doppler signatures," *IET Radar, Sonar & Navigation*, vol. 8, no. 5, pp. 425–434, 2014.

[29] B. Tekeli, S. Z. Gurbuz, and M. Yuksel, "Information-theoretic feature selection for human micro-Doppler signature classification," *IEEE Trans. Geosci. Remote Sens.*, vol. 54, no. 5, pp. 2749–2762, 2016.

[30] F. Costa *et al.*, "Robust reading approach for moving chipless RFID tags by using ISAR processing," *IEEE Trans. Microw. Theory Tech.*, vol. 66, no. 5, pp. 2442–2451, 2017.

[31] A. Azarfar, N. Barbot, and E. Perret, "Towards chipless RFID technology based on micro-Doppler effect for long range applications," in *2021 IEEE MTT-S International Microwave Symposium (IMS)*, Atlanta, US, June 2021.

[32] J. Van Bladel, "Electromagnetic fields in the presence of rotating bodies," *Proc. IEEE*, vol. 64, no. 3, pp. 301–318, 1976.

[33] J. Cooper and C. H. Wilcox, "Scattering by moving bodies: The quasi stationary approximation," *Math. Methods Appl. Sci.*, vol. 2, no. 2, pp. 131–148, 1980.

[34] R. Kleinman and R. Mack, "Scattering by linearly vibrating objects," *IEEE Trans. Antennas Propag.*, vol. 27, no. 3, pp. 344–352, 1979.

[35] R. F. Harrington, *Time-Harmonic Electromagnetic Fields*. Wiley-IEEE Press, 2001, ch. 2.

[36] J. H. Van Vleck, F. Bloch, and M. Hamermesh, "Theory of radar reflection from wires or thin metallic strips," *J. Appl. Phys.*, vol. 18, no. 3, pp. 274–294, 1947.

[37] C. Balanis, *Antenna Theory: Analysis and Design*. Wiley, 2012.

[38] E. Knott, J. Schaeffer, and M. Tulley, *Radar Cross Section*. Institution of Engineering and Technology, 2004, ch. 10.

[39] V. Chen, F. Li, S.-S. Ho, and H. Wechsler, "Micro-Doppler effect in radar: phenomenon, model, and simulation study," *IEEE Trans. Aerosp. Electron. Syst.*, vol. 42, no. 1, pp. 2–21, 2006.

[40] R. F. Harrington, "Theory of loaded scatterers," in *Proc. Inst. Electr. Eng.*, vol. 111, no. 4. IET, 1964, pp. 617–623.

[41] R. Harrington, "Electromagnetic scattering by antennas," *IEEE Trans. Antennas Propag.*, vol. 11, no. 5, pp. 595–596, 1963.

[42] Numerical electromagnics code. [Online]. Available: https://www.nec2.org/

[43] R. Bracewell and R. Bracewell, *The Fourier Transform and Its Applications*, ser. Electrical engineering. McGraw Hill, 2000.

[44] A. Carlson, P. Crilly, and J. Rutledge, *Communication Systems: An Introduction to Signals and Noise in Electrical Communication*. McGraw-Hill, 2002, pp. 190–192.

[45] P. Nikitin, K. Rao, and R. Martinez, "Differential RCS of RFID tag," *Electron. Lett.*, vol. 43, pp. 431 – 432, 02 2007.

[46] N. Barbot, O. Rance, and E. Perret, "Differential RCS of modulated tag," *IEEE Trans. Antennas Propag.*, vol. 2, no. 9, pp. 10–15, 2021.

[47] "SAS-571 data sheet," A.H. Systems, inc, Chatworth, Canada.

Ashkan Azarfar received the B.Sc. from the Iran University of Science and Technology, Tehran, Iran in 2014, and the M.Sc. from the University of Tehran, Tehran, Iran in 2017, both in electrical engineering. He is currently pursuing the Ph.D. degree at the University of Grenoble Alps - Grenoble Institute of Technology, Valence, France. His research interests include EM scattering, antenna design, and microwave circuits.

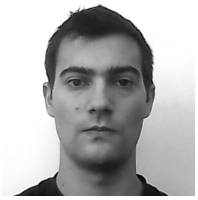

Nicolas Barbot received the M.Sc. degree and Ph.D. degree from the University de Limoges, France. His Ph.D. work in Xlim Laboratory, Limoges, France was focused on error-correcting codes for the optical wireless channel. He also realized a post-doctoral work in joint source-channel decoding at L2S Laboratory, in Gif-sur-Yvette, France. Since September 2014, he has been an Assistant Professor at the Université Grenoble Alpes - Grenoble Institute of Technology, in Valence, France. His scientific background at LCIS Laboratory, Valence, France covers wireless communications systems based on backscattering principle which include classical RFID and chipless RFID.

His research interests include transponders which can not be described by linear time-invariant systems. This gathers harmonic transponders which are based on the use of a non-linear component (Schottky diode) or linear time-variant transponders which are based on the modification of their response in the time domain. He also places special interests on antenna design and instrumentation based on these phenomenons.

Etienne Perret (S'02–M'06–SM'13) received the Eng. Dipl. degree in electrical engineering from the Ecole Nationale Supérieure d'Electronique, d'Electrotechnique, d'Informatique, d'Hydraulique, et des Télécommunications, Toulouse, France, 2002, and the M.Sc. and Ph.D. degrees in electrical engineering from the Toulouse Institute of Technology, Toulouse, in 2002 and 2005, respectively. From 2005 to 2006, he held a post-doctoral position with the Institute of Fundamental Electronics, Orsay, France. In 2006, he was appointed Associate Professor of electrical engineering at Grenoble INP - Institute of Engineering Univ. Grenoble Alpes, France. From 2014 to 2019, he has been a Junior Member with the Institut Universitaire de France, Paris, France, an institution that distinguishes professors for their research excellence, as evidenced by their international recognition. From 2015 to 2020, he has been an Appointed Member of the French National Council of Universities. He has authored or co-authored more than 200 technical conferences, letters and journal papers, and books and book chapters. He holds several patents. His works have generated more than 3500 citations. His current research interests include wireless communication systems based on the principle of backscatter modulation or backscattering of EM waves especially in the field of RFID and chipless RFID for identification and sensors. His research interests also include electromagnetic modeling of passive devices for millimeter and submillimeter-wave applications, and advanced computer-aided design techniques based on the development of an automated codesign synthesis computational approach. Dr. Perret has been a Technical Program Committee member of the IEEE International Conference on RFID, the IEEE RFID TA; and currently he is a member of the IMS Technical Paper Review Committee. He was a recipient of several awards like the MIT Technology Review's French Innovator's under 35 in 2013, the French Innovative Techniques for the Environment Award in 2013, the SEE/IEEE Leon Brillouin Award for his outstanding achievement in the identification of an object in an unknown environment using a chipless label or tag in 2016, the IEEE MTT-S 2019 Outstanding Young Engineer Award, the Prix Espoir IMT – Académie des sciences in 2020 and the Grand Prix de l'Electronique Général Ferrié in 2021. He was a Keynote Speaker and the Chairman of several international symposiums. Etienne Perret was awarded an ERC Consolidator Grant in 2017 for his project ScattererID.